Distributed Temperature Control in Laser-Based Manufacturing

Chengjian Zheng
Bloomberg, Inc.,
New York, NY 10022
e-mail: cj.zheng.91@gmail.com

John T. Wen
Department of Electrical, Computer, and Systems
Engineering,
Rensselaer Polytechnic Institute,
Troy, NY 12180
e-mail: wenj@rpi.edu

Mamadou Diagne[1]
Mem. ASME
Department of Mechanical, Aerospace, and
Nuclear Engineering,
Rensselaer Polytechnic Institute,
Troy, NY 12180
e-mail: diagnm@rpi.edu

Temperature control is essential for regulating material properties in laser-based manufacturing. Motion and power of the scanning laser affect local temperature evolution, which in turn determines the a posteriori microstructure. This paper addresses the problem of adjusting the laser speed and power to achieve the desired values of key process parameters: cooling rate and melt pool size. The dynamics of a scanning laser system is modeled by a one-dimensional (1D) heat conduction equation, with laser power as the heat input and heat dissipation to the ambient. Since the model is 1D, length and size are essentially the same. We pose the problem as a regulation problem in the (moving) laser frame. The first step is to obtain the steady-state temperature distribution and the corresponding input based on the desired cooling rate and melt pool size. The controller adjusts the input around the steady-state feedforward based on the deviation of the measured temperature field from the steady-state distribution. We show that with suitably defined outputs, the system is strictly passive from the laser motion and power. To avoid over-reliance on the model, the steady-state laser speed and power are adaptively updated, resulting in an integral-like update law for the feedforward. Moreover, the heat transfer coefficient to the ambient may be uncertain, and can also be adaptively updated. The final form of the control law combines passive error temperature field feedback with adaptive feedforward and parameter estimation. The closed-loop asymptotical stability is shown using the Lyapunov arguments, and the controller performance is demonstrated in a simulation. [DOI: 10.1115/1.4046154]

1 Introduction

Laser additive manufacturing (LAM) is gaining interest in rapid prototyping, coating, parts repairing etc. due to its ability to generate a wide range of configuration and geometries, through a layer-by-layer melting–solidification process [1]. Although literature has suggested its capability of creating superior properties compared to the wrought material through rapid melting and cooling [2], variabilities and inconsistencies in the fabrication process often degrade the performance of the finished part. As a result, LAM has not been widely applied to critical industries such as aerospace, energy, and automotive [3].

Material properties are largely determined by microstructure. Characterization of microstructure evolution in LAM has been extensively studied [1,2,4–6]. Tight control of the processing conditions is necessary for optimizing the material microstructure, and in turn, physical properties [7,8]. Similar to metallic manufacturing processes, thermal processing is critical to the microstructure of the finished part. Suitable control of the thermal condition could achieve parts with desired hardness, strength, etc. [9]. In Refs. [3] and [10], the thermal control problem is reduced to the regulation of the real-time cooling rate. Thermal control in LAM is similar to that in arc welding [11–14]. Distributed parameter heat transfer models have been developed [13,15,16], and process parameters, such as cooling rate and melt pool size, have been identified as key indicators of the resulting material properties [17,18]. Various methods have been proposed to regulate these parameters by estimating and feedback them back to controlling the motion and power of the scanning laser, including neural network [17], controller design based on identified linear models [14], and direct estimation and feedback of the cooling rating with an IR camera [3]. Recently, multiple tracks and multilayer part

fabrications have been investigated in Refs. [19] and [20] using iterative learning control techniques. In the current literature, proposed models for laser manufacturing processes are open-loop stable and closed-loop control approaches are used to achieve performance requirements and to ensure robustness to perturbations.

In this paper, we propose an alternate approach of temperature control in LAM. We regulate the distributed temperature field in the laser frame, with the target temperature field design based on the desired values of key process parameters such as cooling rate and melt pool size. We model the system dynamics as a one-dimensional (1D) heat conduction problem, with Newtonian heat loss to the ambient and heat input from the moving laser. This is a simplification of the full problem, which is three-dimensional (3D), involves solidification and melting, and contains dynamics of the liquid–solid interface (see Stephan problem [21,22] for the static heat source case). We use the simplified model to develop the control methodology, which would lay the foundation to tackle the more complex full-scale problem. Our approach decomposes the problem into two parts. The first part designs a desired temperature distribution and the corresponding laser input in the laser frame to meet certain criteria, e.g., the cooling rate and melt pool size. By using an energy-like Lyapunov function, we show that the input (deviation from the desired values) to a set of suitably chosen outputs, which depend on the temperature field error, is strictly passive. The Lyapunov approach leads to a large family of stabilizing controllers and also provides the framework for the adaptation of uncertain heat transfer to the ambient. The strict passivity implies that any passive feedback is stabilizing. A particular choice is simply a constant feedback as in proportional control. The constant feedforward portion of the controller depends on the model. It may be estimated based on the temperature field error, resulting in an integral-like term. The proportional-integral (PI) control is a special case of this family of passive-integral stabilizing control laws. When the heat transfer to the ambient is also uncertain, it may be adaptively estimated and incorporated into the control law. The resulting control structure is a passive

temperature field error feedback combined with an integral control estimating the feedforward laser speed and power and an adaptation term for the heat transfer coefficient of the ambient heat loss. We use the 1D partial differential equation (PDE) model as the truth model for evaluating the controller performance. For computation, we use the truncated modal expansion as an approximation of the full model. For controller design and stability analysis, we use the moving laser frame by applying a coordinate transformation similar to [11], resulting in a reaction–advection–diffusion equation. Simulation results of open-loop response and closed-loop response with and without incorporating the estimation of heat transfer coefficient α are presented as demonstration of the proposed control strategies. The PDE model is parabolic, which may be approximated by a finite dimensional ordinary differential equation (ODE), e.g., using the modal coordinate. With the laser motion and power as input variables, the control problem contains a bilinear advective term, which is a key challenge addressed in this paper.

This paper is organized as follows: In Sec. 2, we discuss the derivation of the 1D PDE model. Section 3 presents the formulation of the control problem, optimization based on different criteria for desired temperature field evolution, and statement of the control objective. Section 4 describes the control design to achieve set point regulation, and in turn, the desired cooling rate and melt pool size. Section 5 presents the simulation results. Section 6 concludes the paper.

2 Temperature Evolution Model

2.1 Inertial Frame Model. Within a single scan, we approximate the system dynamics in terms of the temperature distribution in a rod along the scanning direction (as shown in Fig. 1). This rod may be considered as the active volume where crucial thermal (and microstructure) evolution occurs. Let the cross-sectional area and perimeter of the rod be $\bar{S}$ and $\bar{A}$. Denote the temperature distribution along the scan direction, x, by $T(x, t)$. The rod is heated by a moving laser heat source with power $P(t)$ with the laser beam centered at $s(t) = s_0 + \int_0^t v(\tau)d\tau$, where s_0 denotes the initial position and $v(t) \geq 0$ the scanning speed. Represent the laser power distribution by a function $\Pi(y)$ where $y = x - s(t)$ is the position relative to the laser beam center. Commonly used laser power distribution includes δ distribution [17], rectangular function

$$\Pi(y) = \frac{1}{D}\text{rect}\left(\frac{y}{D}\right) = \begin{cases} \dfrac{1}{D}, & |y| < \dfrac{D}{2} \\ \dfrac{1}{2D}, & |y| = \dfrac{D}{2} \\ 0, & |y| > \dfrac{D}{2} \end{cases} \tag{1}$$

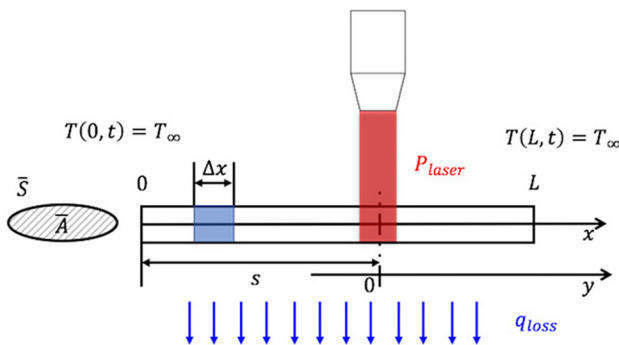where D is the effective diameter of laser beam, and the Gaussian power distribution [15]

Fig. 1 One-dimensional domain of a single laser scan

$$\Pi(y) = \mathcal{N}(0, \sigma) = \frac{1}{\sigma\sqrt{2\pi}}e^{-\frac{y^2}{2\sigma^2}} \tag{2}$$

Heat generated by the laser conducts along the x direction, and also transfers through the lateral surface of the rod. This work only focuses on temperature variation along the laser scanning direction; we approximate the lateral heat loss by a lumped heat sink with Newton's law of cooling: $q_{\text{loss}} = \beta(T - T_\infty)$ where T_∞ is the ambient temperature and β is a heat transfer coefficient. In free-form additive manufacturing, β may be both spatial and time dependent, caused by different cooling conditions in different structures and materials. This is a key source of disturbance affecting the temperature distribution.

In a thin slice of the rod of thickness Δx, by the conservation of energy, we have

$$\frac{\Delta x \bar{A} \rho C_p\big(T(t + \Delta t) - T(t)\big)}{\Delta t}$$
$$= \bar{k}\bar{A}\big(T_x(x + \Delta x) - T_x(x)\big) - \bar{S}\Delta x q_{\text{loss}} + Q(x, t)\Delta x \tag{3}$$

where $\bar{k}$, C_p, and ρ are, respectively, thermal conductivity, specific heat, and density. The subscript in T_x denotes $(\partial T/\partial x)$. The volumetric heat flux due to the moving laser, $Q(x, t)$, is

$$Q(x, t) = \kappa P(t)\Pi(x - s) \tag{4}$$

where $\kappa \in (0, 1)$ denotes the laser energy transfer efficiency, which is usually between 30% and 50% [23]. Define $u(x, t) = T(x, t) - T_\infty$. With $\Delta x \to 0$, Eq. (3) becomes

$$u_t(x, t) = ku_{xx}(x, t) - \alpha u(x, t) + p(t)\Pi(x - s(t)) \tag{5}$$

where

$$k = \frac{\bar{k}}{\rho C_p}, \quad p(t) = \frac{\kappa P(t)}{\bar{A}D\rho C_p}, \quad \alpha = \frac{\bar{S}\beta}{\bar{A}\rho C_p}$$

Material-related parameters k and κ are usually known, but the heat-loss coefficient α is unknown and possibly varying with time and position. Assuming a long rod with both ends held at the ambient temperature. As an approximation, we use a Dirichlet boundary condition $u(-\ell, t) = u(\ell, t) = 0$ for a sufficiently large ℓ. Also, assume that the rod is initially in equilibrium with the ambient: $u(x, 0) = 0$. Consider the laser velocity as the input; then the laser position s is given by

$$\dot{s}(t) = v(t), \quad s(0) = s_0 \tag{6}$$

Equations (5) and (6) describe the control model, with $(u(x, t), s(t))$ as the state and $(v(t), p(t))$ as the input.

2.2 Laser Frame Model. Since the laser constantly moves, stability is not meaningful in the inertial frame. Instead, we convert the dynamics to the laser frame, similar to Ref. [11]. Define a coordinate system attached to the laser:

$$y(t) = x - s(t) \tag{7}$$

Define the temperature distribution in the laser frame as

$$U(y, t) := u(y + s(t), t) = u(x, t) \tag{8}$$

Note that $U_y(y, t) = u_x(x, t)$. Hence, $U_{yy}(y, t) = u_{xx}(x, t)$ and

$$U_t(y, t) = \frac{\partial}{\partial t}U(y, t) = v(t)\frac{\partial}{\partial x}u(y + s(t), t) + \frac{\partial}{\partial t}u(y + s, t)$$
$$= v(t)U_y(y, t) + u_t(y + s, t)$$

Substituting into Eq. (5), we obtain an advection–diffusion–reaction equation

$$U_t = kU_{yy} + v(t)U_y - \alpha U + p(t)\Pi(y) \tag{9}$$

For the boundary condition, assume that the temperature is at ambient sufficiently far away from the laser, i.e., $U(-L, 0) = U(L, 0) = 0$, for L sufficiently large.

2.3 Steady-State Solution in Laser Frame. For constant laser speed and power, $(v(t), p(t)) = (v^*, p^*)$, we can solve for the steady-state temperature distribution $U^*(y)$ by setting $U_t(y, t)$ to zero in Eq. (9)

$$kU^*_{yy}(y) + v^*U^*_y(y) - \alpha U^*(y) + p^*\Pi(y) = 0$$
$$U^*(-L) = U^*(L) = 0 \tag{10}$$

This is a linear nonhomogeneous ODE, and may be readily solved. Analytical solutions for three typical input laser profiles, delta, rectangular, and Gaussian functions, are derived in Appendix A. Furthermore, this equilibrium is globally exponentially stable as shown below.

THEOREM 1. *Given the temperature evolution equation in the laser frame (9) with constant laser speed and power input (v^*, p^*), the equilibrium U^* given by Eq. (10) is globally exponentially stable.*

Proof. Consider the Lyapunov function candidate

$$V_1 = \frac{1}{2}\int_{-L}^{L} \tilde{U}(y, t)^2 dy \tag{11}$$

where $\tilde{U}(y, t) := U(y, t) - U^*(y)$. The derivative of V along Eq. (9) and with the help of Eq. (10) is written as follows:

$$\begin{aligned}
\dot{V}_1 &= \int_{-L}^{L} \tilde{U}(y, t)\big(kU_{yy}(y, t) + v^*U_y(y, t) - \alpha U(y, t) + p^*\Pi(y)\big)dy \\
&= \int_{-L}^{L} \tilde{U}(y, t)\big(k\tilde{U}_{yy}(y, t) + v^*\tilde{U}_y(y, t) - \alpha\tilde{U}(y, t)dy \\
&= k\Big[\tilde{U}(y, t)\tilde{U}_y(y, t)\Big]_{-L}^{L} - k\int_{-L}^{L}\tilde{U}_y(y, t)^2 dy \\
&\quad + \frac{1}{2}v^*\Big[\tilde{U}(y, t)^2\Big]_{-L}^{L} - \alpha\int_{-L}^{L}\tilde{U}_y(y, t)^2 dy \\
&= -k\int_{-L}^{L}\tilde{U}_y(y, t)^2 dy - \alpha\int_{-L}^{L}\tilde{U}_y(y, t)^2 dy
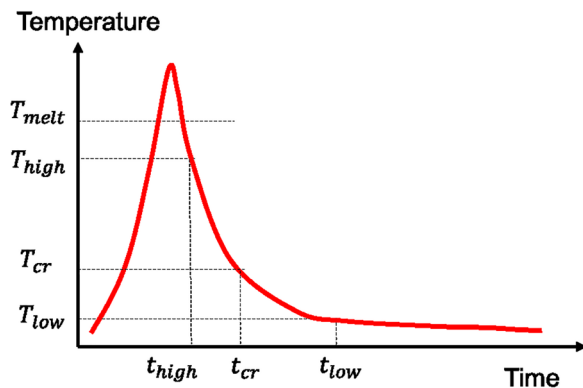\end{aligned}$$
$$\tag{12}$$

Hence, we get

Fig. 2   Typical thermal history of a fixed point on the part

$$\dot{V} \leq -2\alpha V \tag{13}$$

It follows that $V(t) \leq e^{-2\alpha t}V(0)$. Therefore, the equilibrium $U^*(y)$ is globally exponentially stable. ∎

3   Control Problem Formulation

The control problem is to adjust laser speed and power, (v, p) in order to achieve a desired temperature field evolution $u^*(x, t)$. LAM and welding literature points to two critical temporally and spatially varying process parameters, cooling rate and melt pool size:

(1) *Cooling rate*: For each x, the thermal history $u^*(x, t)$ directly determines the microstructure evolution at x, and hence the final material properties. Cooling rate is a widely adopted criterion for designing this thermal history [10,14].
(2) *Melt pool size*: For each t, the temperature distribution around the laser $u^*(x, t)$ affects the surface morphology of the finished part. The melt pool size is determined by the speed of propagation of the solidification front, and consequently affects the geometric integrity of the final part shape. It has been used in the welding [18] and laser additive manufacturing [24] literature to characterize geometric consistency.

Our goal is to regulate both parameters to achieve consistent microstructure and part geometry. If the objectives cannot be met simultaneously because of constraints in scanning speed and laser power, we form a linear combination of the objectives with a tunable parameter to specify the relative emphasis of the objectives. This section will discuss the characterization of these two criteria and the corresponding control problem formulation.

3.1   Cooling Rate. Figure 2 illustrates the typical thermal history at a specific point on the part. The laser heats up the part beyond melting and the part cools as the laser moves away. The cooling history is critical to the determination of the final material microstructure. Following Ref. [25], we define the cooling rate as the time rate of change at a critical temperature

$$\text{Cr}(x) = -\frac{\partial u}{\partial t}(x, t)\Big|_{t=t_{\text{cr}}} \tag{14}$$

where $u(x, t_{\text{cr}}(x)) = T_{\text{cr}}$ and $\frac{\partial u}{\partial t}(x, t)\big|_{t=t_{\text{cr}}} < 0$. The cooling rate only accounts for one single point on the cooling curve (see Fig. 2) and is easy to implement in closed-loop control. Its value at the point of solidification is important to the microstructure, so T_{cr} is typically chosen as the solidification temperature. Cooling rate is by its nature a posteriori and *location-based* as it is characterized by the thermal history at a specific location. An illustration of the concept of Cr(x) is shown in Fig. 3(a). To obtain Cr(x) at $x = \bar{x}$, one needs to first get the temperature history $u(\bar{x}, t)$, find $t_{\text{cr}}(\bar{x})$, and then compute the time derivative at that point.

In contrast to the location-based cooling rate, Refs. [14], [17], and [18] proposed a *time-based* cooling rate, which is the time derivative at the current critical temperature position $x_{\text{cr}}(t)$

$$\text{Cr}(t) = -\frac{\partial u}{\partial t}(x, t)\Big|_{x=x_{\text{cr}}(t)} \tag{15}$$

where x_{cr} is defined as the part location currently at the critical temperature

$$u(x_{\text{cr}}(t), t) = T_{\text{cr}} \tag{16}$$

Figure 3(b) shows the definition of Cr(t). To obtain Cr(t) for $t = \bar{t}$, one needs to get $x_{\text{cr}}(\bar{t})$ from the current temperature snapshot $u(x, \bar{t})$, then compute $\text{Cr}(x_{\text{cr}}(\bar{t}))$ following the procedures of location-based cooling rate mentioned above. Transformed into the laser frame, Eq. (15) becomes
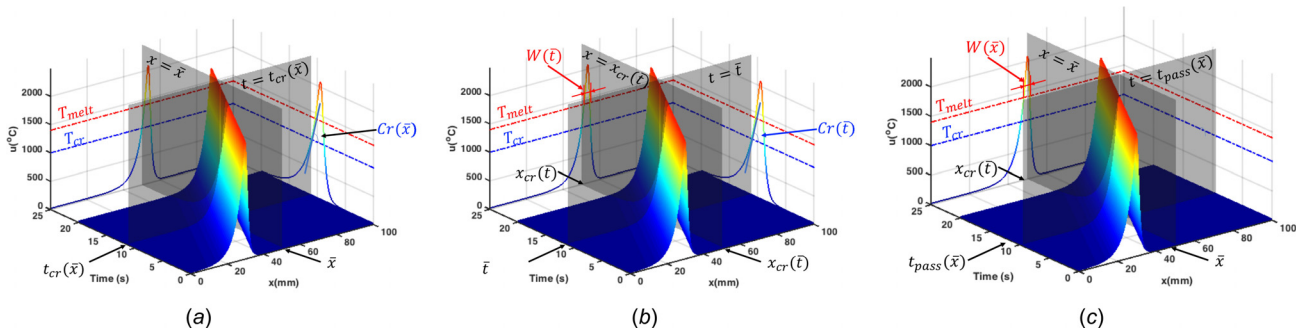
Fig. 3 Definition of melt pool size and cooling rate defined with respect to location and time. (*a*) Explains Cr(x) for a spatial position $x = \bar{x}$. (*b*) Presents Cr(t) and W(t) for a time instance $t = \bar{t}$. (*c*) Illustrates W(x) for a spatial position $x = \bar{x}$.

$$
\begin{aligned}
\mathrm{Cr}(t) &= -\frac{\partial}{\partial t} U(y(t), t)|_{y(t)=y_{\mathrm{cr}}} \\
&= (U_y(y, t)v(t) - U_t(y, t))|_{y=y_{\mathrm{cr}}}(t) \\
&:= F(U(t), v(t))
\end{aligned}
\tag{17}
$$

where y_{cr} is the part location in the laser frame at the critical temperature: $U(y_{\mathrm{cr}}, t) = T_{\mathrm{cr}}$.

3.2 Melt Pool Size. To achieve uniform part quality, the average temperature in the melt pool [10] or the size of the melt pool [14] has been identified as critical parameters. Originally, melt pool size W is defined as the width of the melt pool along the direction perpendicular to the scanning direction, which directly determines the geometry and size of the finished clad [26], and hence the overall surface morphology of the finished part. However, in 1D model, we can only use the size along the scanning direction as a proxy. At each t, define the melt pool as

$$
\begin{aligned}
\mathcal{W}(t) &= \{x \in [-\ell, \ell] : u(x, t) \geq T_{\mathrm{melt}}\} \\
&= \{y \in [-L, L] : U(y, t) \geq T_{\mathrm{melt}}\}
\end{aligned}
$$

The melt pool size $W(t)$ at each time instance t is then

$$
W(t) = \max_{y \in \mathcal{W}(t)} y - \min_{y \in \mathcal{W}(t)} y := G(U)
\tag{18}
$$

Note that $\mathcal{W}$ may be similarly defined using U, resulting in the same W. If the peak temperature is lower than T_{melt}, $\mathcal{W}$ is empty. In that case, $W = 0$.

We also characterize the melt pool size, $W(x)$, corresponding to a given location x, as the melt pool size when the laser passes through x.

Define the time when the laser passes through x as $t_{\mathrm{pass}}(x)$, i.e., $x = s(t_{\mathrm{pass}}(x))$. The location-based melt pool size is then defined as

$$
W(x) = W(t_{\mathrm{pass}}(x))
\tag{19}
$$

3.3 Design of Steady-State Temperature Distribution. As shown in Sec. 2.3, for constant (v^*, p^*), $U(y, t)$ converges to a steady temperature distribution $U^*(y)$ exponentially. We now choose (v^*, p^*) based on desired cooling rate and melt pool size. For the cooling rate, we use the time-based cooling rate (17). Given $U^*(y)$ (corresponding to specified (v^*, p^*)), it becomes

$$
\mathrm{Cr}^* = U_y^*(y_{\mathrm{cr}})v^*, \quad U^*(y_{\mathrm{cr}}) = T_{\mathrm{cr}}
\tag{20}
$$

where T_{cr} is a specified critical temperature, and y_{cr} is define with the implicit equation above. The weld pool size corresponding to U^* is given by

$$
\begin{aligned}
\mathcal{W}^* &= \{y : U^*(y) \geq T_{\mathrm{melt}}\} \\
W^* &= \max \mathcal{W}^* - \min \mathcal{W}^*
\end{aligned}
\tag{21}
$$

The steady-state temperature design is now posed as a static optimization problem.

Given desired cooling rate and melt pool size, $(\mathrm{Cr}_{\mathrm{des}}, W_{\mathrm{des}})$, (Cr^*, W^*) from Eqs. (20) and (21), and constant weights (w_1, w_2), find (v^*, p^*), $v^* \in [0, v_{\mathrm{max}}]$, $p^* \in [0, p_{\mathrm{max}}]$, to minimize

$$
J = w_1(\mathrm{Cr}^* - \mathrm{Cr}_{\mathrm{des}})^2 + w_2(W^* - W_{\mathrm{des}})^2
\tag{22}
$$

In general, this problem may be numerically solved. In the case of $\Pi(y) = \delta(y)$, (v^*, p^*) may be analytically related to the specified (Cr^*, W^*) (given by Eqs. (B1) and (B4), as shown in Appendix 6). Denote the solution as

$$
v^* = f(\alpha, \mathrm{Cr}_{\mathrm{des}}), \quad p^* = g(\alpha, v^*, W_{\mathrm{des}})
$$

where the dependence on α is highlighted. These expressions may be used as an approximation of rectangular power input function. As shown in Fig. 4, $U^*(y)$s corresponding to the delta function and rectangular function of various width D are reasonably close.

3.4 Control Objective. The control objective is to drive the temperature distribution in the laser frame $U(y, t)$ to the desired $U^*(y)$ by adjusting the laser speed and power (v, p) based on the measured $U(y, t)$. The desired $U^*(y)$ is designed based on the specified desired cooling rate and weld pool size, $(\mathrm{Cr}_{\mathrm{des}}, W_{\mathrm{des}})$ as described in Sec. 2.3. The measurement of the temperature distribution $U(y, t)$ may be performed with an IR camera mounted with the laser. The control objective needs to be robust with respect to
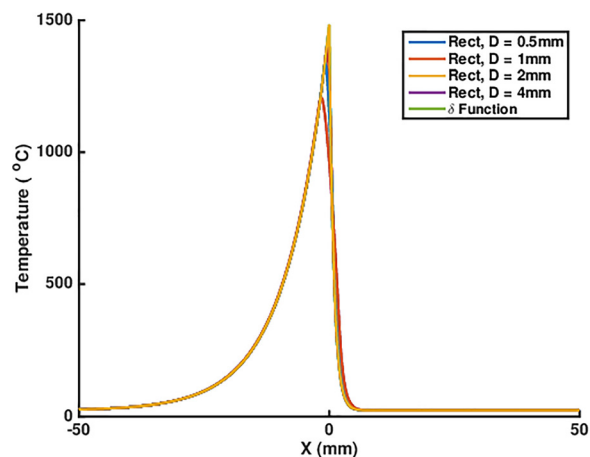

Fig. 4 Analytical solution of the steady-state under rectangular laser power distribute on function $\Pi(X)$ defined by Eq. (1)

unmodeled disturbances, such as stray ambient heat, model uncertainties, such as the heat transfer coefficient, α, for loss to the ambient, and nonzero initial conditions.

4 Control Design

4.1 Passivity-Based Output Feedback. With $U^*(y)$ given by Eq. (10) (and (v^*, p^*) computed based on (Cr_{des}, W_{des})), the temperature error is governed by

$$\tilde{U}_t(y,t) = k\tilde{U}_{yy}(y,t) - \alpha\tilde{U}(y,t) + v\tilde{U}_y(y,t)$$
$$+\tilde{v}(t)U_y^*(y,t) + \tilde{p}(t)\Pi(y) \tag{23}$$

$$\tilde{U}(-L,0) = \tilde{U}(L,0) = 0 \tag{24}$$

where

$$\tilde{U}(t) = U(y,t) - U^*(y), \quad \tilde{v}(t) = v(t) - v^*, \quad \tilde{p}(t) = p(t) - p^*$$

If (v^*, p^*) are known, we show that $(\tilde{v}(t), \tilde{p}(t))$ is strictly passive [27] with respect to certain specified outputs.

PROPOSITION 1. *The temperature error system (23) is strictly passive with respect to inputs $(\tilde{v}(t), \tilde{p}(t))$ and outputs (y_v, y_p) given by*

$$y_v(t) = \int_{-L}^{L} \tilde{U}(y,t)U_y^*(y)dy \tag{25a}$$

$$y_p(t) = \int_{-L}^{L} \tilde{U}(y,t)\Pi(y)dy \tag{25b}$$

Proof. The statement follows from the same Lyapunov analysis as in the proof of Theorem 1. Taking the derivative of the Lyapunov function (11) along Eqs. (23) and (24), one gets

$$\dot{V}_1 = -k\int_{-L}^{L} \tilde{U}_y(y,t)^2 dy - \alpha\int_{-L}^{L} \tilde{U}(y,t)^2 dy$$
$$+\tilde{v}(t)\int_{-L}^{L} \tilde{U}(y,t)U_y^*(y)dy + \tilde{p}(t)\int_{-L}^{L} \tilde{U}(y,t)\Pi(y)dy$$

Integrating both sides, the stated strict passivity property follows. ∎

It then follows that with any passive feedback, the system remains globally exponentially stable, as shown below.

THEOREM 2. *Given the feedback control law*

$$\tilde{v}(t) = -\mathcal{K}_v y_v(t), \quad \tilde{p}(t) = -\mathcal{K}_p y_p(t) \tag{26}$$

where $\mathcal{K}_v$ and $\mathcal{K}_p$ are passive maps and $(y_v(t), y_p(t))$ is defined in Eq. (25), the closed-loop system (23) is globally exponentially stable.

Proof. Substituting Eq. (26) into $\dot{V}$ in the proof of Proposition 1, we have

$$\dot{V} \leq -2\alpha V - y_v\mathcal{K}_v y_v - y_p\mathcal{K}_p y_p$$

Integrating both sides and applying the passivity property of $\mathcal{K}_v$ and $\mathcal{K}_p$, it follows that the zero equilibrium, $\tilde{U} = 0$, is globally exponentially stable. ∎

A common choice of $\mathcal{K}_v$ and $\mathcal{K}_p$ is simply a constant gain, which results in a proportional output feedback control law.

4.2 Estimation of (v^*, p^*): Integral Control. The control law (26) requires the knowledge of (v^*, p^*). If they are uncertain or unknown, they may be estimated using the same Lyapunov analysis as before. The result is summarized below.

THEOREM 3. *Consider the feedback control law*

$$v(t) = \hat{v}^* - \mathcal{K}_v y_v(t), \quad p(t) = \hat{p}^* - \mathcal{K}_p y_p(t) \tag{27a}$$

$$\dot{\hat{v}}^* = -K_{I_v}y_v(t), \qquad \dot{\hat{p}}^* = -K_{I_p}y_p(t) \tag{27b}$$

Then the zero equilibrium of the closed-loop system (23) is globally asymptotically stable.

The controller structure from the above is essentially PI control with output feedback of (y_v, y_p). This control law means that the temperature distribution $U(y, t)$ would still converge to $U^*(y)$, despite the possible use of an erroneous model and (v^*, p^*).

Remark 1. The control design relies on the real-time measurement of the distributed temperature along with the spatial domain. This may be obtained using an infrared camera [3]. In Ref. [28], acoustic and electromagnetic signatures are used to measure temperature as well as the thermal history of materials. Standard CCD or CMOS image arrays have also been used to estimate melt pool shape and temperature profiles [29–33].

4.3 Estimation of α. If the model is erroneous, then $U^*(y)$ may not correspond to our ultimate control objective of regulating $(Cr(t), W(t))$. We consider the case where the major model uncertainty is the heat transfer coefficient α. In this case, we construct an estimator for α by replicating the nominal plant. The convergence property of the estimator is summarized below.

PROPOSITION 2. *Let $\hat{U}(y,t)$ be the solution of*

$$\hat{U}_t(y,t) = k\hat{U}_{yy}(y,t) + v(t)\hat{U}_y(y,t) - \hat{\alpha}\hat{U}(y,t) + p(t)\Pi(y)$$
$$+K_e(U(y,t) - \hat{U}(y,t)) \tag{28}$$

$$\hat{U}(-L,t) = \hat{U}(L,t) = 0 \tag{29}$$

where $\hat{\alpha}$ is updated with

$$\dot{\hat{\alpha}}(t) = \gamma\int_{-L}^{L} \hat{U}(y,t)(U(y,t) - \hat{U}(y,t)dy \tag{30}$$

Then $|\hat{U} - U|$ converge to zero as $t \rightarrow \infty$.

Proof. Define the Lyapunov function candidate

$$V_2 = \frac{1}{2}\int_{-L}^{L} \check{U}(y,t)^2 dy + \frac{1}{2\gamma}\check{\alpha}^2(t)$$

where $\check{U}(y,t) := U(y,t) - \hat{U}(y,t)$, $\check{\alpha} := \alpha - \hat{\alpha}$ and γ is a positive gain parameter. The derivative along Eqs. (9), (28), and (30) is written as follows:

$$\dot{V}_2 = \int_{-L}^{L} k\check{U}(y,t)\check{U}_{yy}(y,t)dy - (\alpha + K_e)\int_{-L}^{L} \check{U}(y,t)^2 dy$$
$$+v(t)\int_{-L}^{L} \check{U}(y,t)\check{U}_y(y,t)dy + \check{\alpha}(t)\int_{-L}^{L} \check{U}(y,t)\hat{U}(y,t)dy$$
$$-\gamma^{-1}\check{\alpha}(t)\dot{\hat{\alpha}}(t)$$
$$= -k\int_{-L}^{L} \check{U}_y(y,t)^2 dy - (\alpha + K_e)\int_{-L}^{L} \check{U}(y,t)^2 dy$$

Note that the terms involving $\check{\alpha}$ are canceled with the choice of the $\hat{\alpha}$ update rule (30). Integrating both sides and applying Barbalat's Lemma [27], it follows that $|\check{U}| \rightarrow 0$ as $t \rightarrow \infty$. ∎

As typical in parameter estimation, additional persistent excitation condition [27] on $\hat{U}$ needs to be satisfied to ensure the convergence of $\hat{\alpha}$ to α. Since there is only one parameter to estimate (α is a scalar), this condition is satisfied unless the system is already at steady-state. The estimator involves the solution of a partial differential equation. Any numerical scheme may be used, e.g., the finite difference method or the proper orthogonal decomposition with the eigenfunctions of $k(\cdot)_{yy}$ as the basis of the projection (described in Sec. 5.1).

4.4 Overall Control Structure. The overall control system is shown in Fig. 5. The estimator (28)–(30) generates $\hat{\alpha}(t)$, which
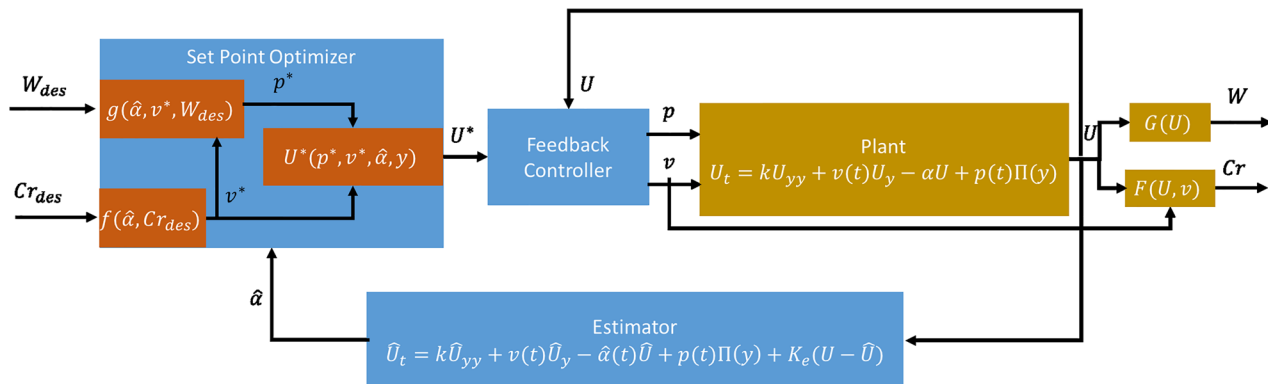
Fig. 5 The structure of control design

feeds into the setpoint optimizer (as described in Sec. 3.3) to compute $U^*(y)$. The feedback controller uses the measured and target temperature distribution, $U(y, t)$ and $U^*(y)$, to updates the laser speed and power, $(v(t), p(t))$, as in Eq. (27).

5 Simulation Results

5.1 Simulation Model. A variety of numerical schemes may be used to compute the solution of Eqs. (5) and (6) under input (v, p). In this paper, we apply the modal approximation using the natural mode of the unforced system (see Appendix 6). Express $u(x, t)$ in the modal basis for each t

$$u(x, t) = \sum_{i=0}^{\infty} q_i(t)\phi_i(x) \tag{31}$$

Projecting Eq. (5) onto ϕ_i, we have

$$\dot{q}_i = -(\lambda_i + \alpha)q_i + b_i(s)p, \quad q_i(0) = 0 \tag{32}$$

The ith input coefficient $b_i(s)$ is given by

$$b_i(s) = \langle \phi_i, \Pi(\cdot - s) \rangle = \int_0^\ell \phi_i(x)\Pi(x - s)\, dx \tag{33}$$

where $\langle \cdot, \cdot \rangle$ denotes the $L_2[0, \ell]$ inner product. For the delta function laser input, $b_i(s) = \phi_i(s)$. For the rectangular laser pulse

$$b_0 = \frac{D}{\sqrt{\ell}}, \quad b_i = \frac{2\sqrt{2\ell}}{i\pi}\sin\left(\frac{i\pi D}{2\ell}\right)\sin\left(\frac{i\pi s}{2\ell}\right), \quad i > 0 \tag{34}$$

For the Gaussian laser pulse, b_is may be computed by numerical integration. For the simulation results presented in this section, we approximate $u(x, t)$ by the first N modes, where N is determined by a specified convergence criterion. Because of the moving heat source and the large domain size ℓ, a large N is typically needed.

5.2 Choice of Parameters. The material for simulation is chosen as stainless steel 316 (as in Ref. [3]). Table 1 lists the material properties used in the simulation. The critical microstructure evolution during cooling of stainless 316 happens between $700\,°C$ and $1300\,°C$ [10]. We choose the midpoint of this temperature range as the critical temperature ($T_{cr} = 1000\,°C$) for measuring *type-II* cooling rate. Other nonmaterial-related simulation parameters are provided in Table 2. We select $\bar{A}$, $\bar{S}$, β (and the associated α) to match the experimental results in Ref. [3]. A comparison of the steady-state melt pool temperature and cooling rate between the 1D model simulation and the experimental data from Ref. [3] is shown in Fig. 6. The extraction of these values from the simulated data follows the description in Ref. [3]. The

Table 1 Material-related parameters

Parameter	Value
k'	$1.3 \times 10^{-2}\,\mathrm{W\,m^{-1}\,K^{-1}}$
C_p	$490\,\mathrm{J\,kg^{-1}\,K^{-1}}$
ρ	$7.87 \times 10^{-6}\,\mathrm{kg\,mm^{-3}}$
T_{melt}	$1400\,°C$
T_{cr}	$1000\,°C$

Table 2 Other simulation parameters

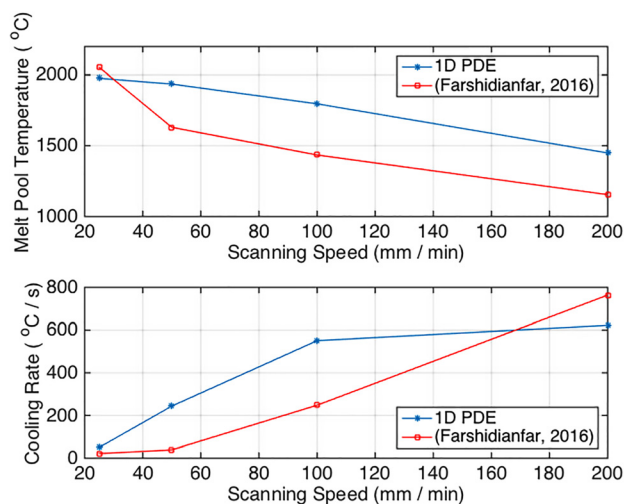| Parameter	Value
κ	50%
$\bar{A}$	$11\,\mathrm{mm^2}$
$\bar{S}$	$20\,\mathrm{mm}$
β	$0.6\,\mathrm{J\,mm^{-2}\,K^{-1}}$
T_∞	$21\,°C$
ℓ	$100\,\mathrm{mm}$
s_0	$20\,\mathrm{mm}$
N	200
Δt	$0.01\,\mathrm{s}$
α	0.7

Fig. 6 Comparison of the steady-state response of the maximum melt pool temperature and cooling rate between 1D simulation and experimental data from Ref. [3]
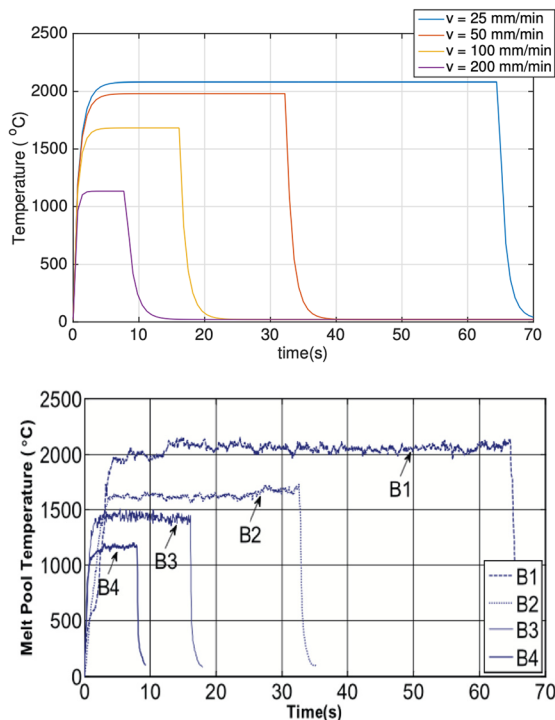
Fig. 7 Comparison of the transient response of the maximum melt pool temperature between 1D simulation and experimental data (B1: v = 25 mm/min, B2: v = 50 mm/min, B3: v = 100 mm/min, B4: v = 200 mm/min. Experimental plot is from Fig. 9 in Ref. [3]).
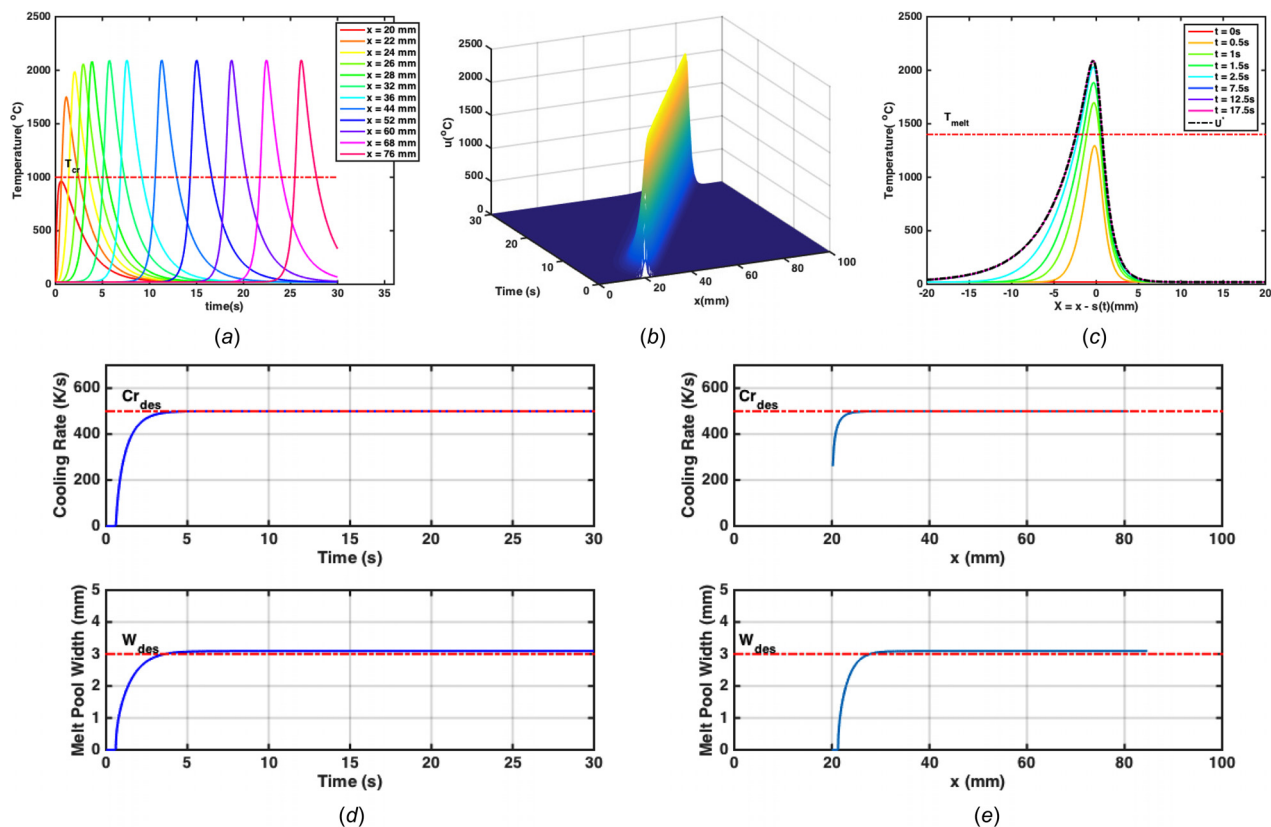
maximum temperature is used as the melt pool temperature (corresponding to the maximum pixel temperature in the infrared image used in the experiments). The cooling rate is calculated based on the change of the maximum temperature at $\Delta T = 0.91$ s apart. The comparison between the transient responses of the melt pool temperature under various scanning speed is shown in Fig. 7. The simulation captures the trend of melt pool temperature and cooling rate versus scanning speed, and the time constant of the transient response. However, there are significant differences in numerical values. The discrepancies may be due to the 3D heat transfer and melting and solidification process ignored 1D model approximation.

The desired cooling rate for simulation is chosen as $\mathrm{Cr}_{\mathrm{des}} = 500\,\mathrm{K\,s^{-1}}$, which corresponds to an a posteriori hardness of 258 HV1000 [10]. The desired melt pool size for simulation is chosen as $W_{\mathrm{des}} = 3$ mm. In practice, choice of W_{des} needs to consider the two-dimensional spacing between the adjacent laser scans, or the desired width of the finished part when building a thin-wall structure.

5.3 Open-Loop Response to Optimized Input. We first present the simulation results on open-loop response, as shown in Fig. 8. In this case, $\alpha = 0.7$ is correctly known. The inputs are chosen as time-constant values optimized based on $\mathrm{Cr}_{\mathrm{des}}$, W_{des}, and (B1), (B4): $v = v^* = 129.32$ mm/min, $P = \bar{A}D\rho C_p p^*/\kappa = 768.32$ W. As shown in Table 2, on a 100 mm long part, the laser starts from $s_0 = 20$ mm. Initial condition for temperature is set at ambient. To exclude the effect of boundaries, the area of interest for temperature control is from $x = 20$ mm to $x = 80$ mm. The simulation is terminated at $t = 30$ s, before which the location-specific cooling rate and melt pool size over the entire area of interest become valid.

Fig. 8 Open-loop response under optimized control inputs when $\alpha = 0.7$ is correctly known. $v = v^* = 129.32$ mm/min, $P = \bar{A}D\rho C_p p^*/\kappa = 768.32$ W. (b) plots the full temperature field evolution. (a) and (c) plot, respectively, the temperature evolution at specific spatial location x's and the temperature distribution snapshots at specific time instance t's. (d) plots the evolution of cooling rate and melt pool size. (e) shows the a posteriori spatial distribution of cooling rate and melt pool size. The area of interest for temperature control is from $x = 20$ mm to $x = 80$ mm.
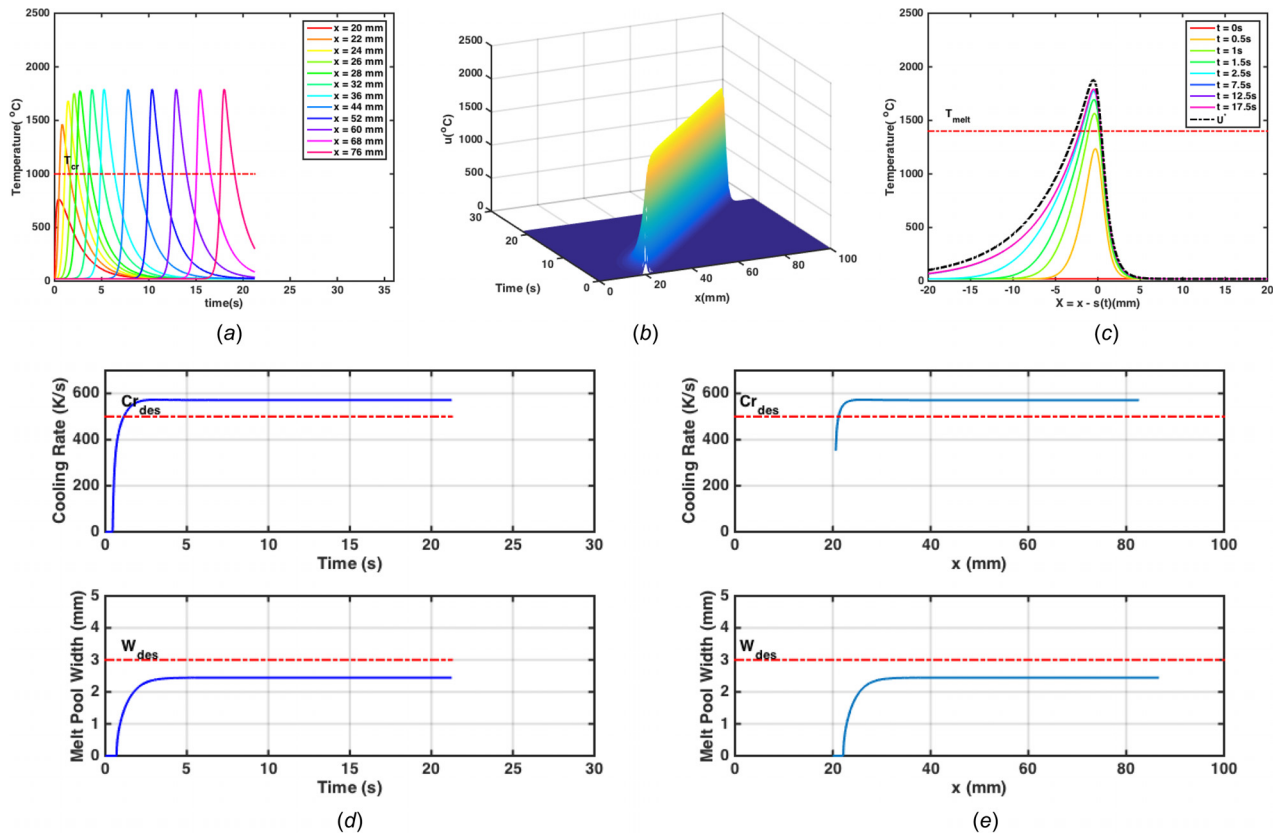
Fig. 9 Open-loop response under optimized control inputs when the known $\hat{\alpha} = 0.6$ but the true $\alpha = 0.7$. $v = v^* = 188.30$ mm/min, $P = \bar{A}D\rho C_p p^*/\kappa = 757.93$ W. (*b*) plots the full temperature field evolution. (*a*) and (*c*) plot, respectively, the temperature evolution at specific spatial location *x*'s and the temperature distribution snapshots (represented in the moving laser frame) at specific time instance *t*'s. (*d*) plots the evolution of cooling rate and melt pool size. (*e*) shows the a posteriori spatial distribution of cooling rate and melt pool size. The area of interest for temperature control is from $x = 20$ mm to $x = 80$ mm.
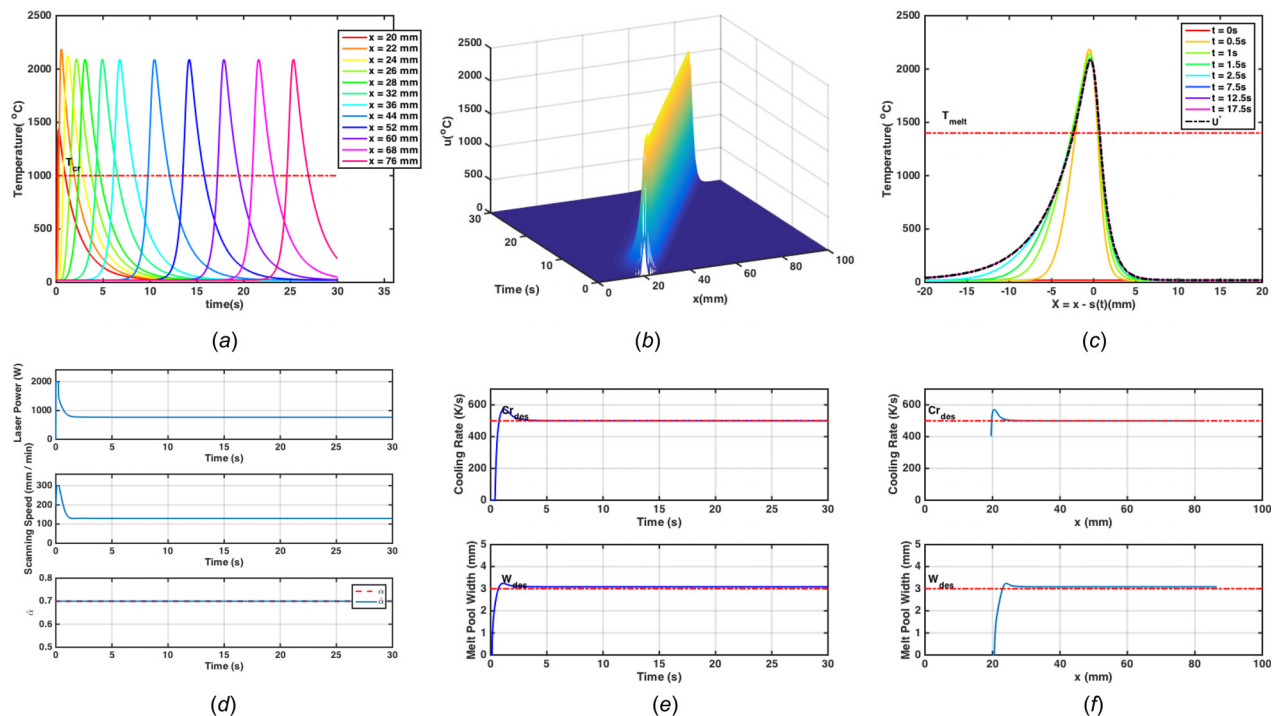

Fig. 10 Closed-loop response with U^* computed from the correctly known $\alpha = 0.7$. (*b*) plots the full temperature field evolution. (*a*) and (*c*) plot, respectively, the temperature evolution at specific spatial location *x*'s and the temperature distribution snapshots at specific time instance *t*'s. (*d*) shows the input response. (*e*) plots the evolution of cooling rate and melt pool size. (*f*) shows the a posteriori spatial distribution of cooling rate and melt pool size. The area of interest for temperature control is from $x = 20$ mm to $x = 80$ mm.

Table 3 Gains selection

$\mathcal{K}_v$	K_{I_v}	$\mathcal{K}_p$	K_{I_p}	γ	K_e
1.2×10^{-3}	8×10^{-5}	8×10^{3}	100	7×10^{-3}	300

Figure 8(b) shows the full temperature field evolution as a three-dimensional surface. Plots in Fig. 8(a) are two-dimensional slices of the three-dimensional surface with respect to specific locations, representing their temperature histories. Figure 8(c) plots the temperature field snapshots (slides with respect to specific time instances) in the (moving) laser frame. Based on all these slices, location-based and time-based cooling rate and melt pool size are then calculated and plotted in Figs. 8(d) and 8(e). It can be seen that after about 4 s, the temperature distribution in the laser frame goes to the steady-state U^*. The time-based cooling rate $Cr(t)$ and melt pool size $W(t)$ also reach steady-state after, respectively, around 3 s and 4 s. Note that a small steady-state error exists due to using delta laser pulse as approximation for solving the optimal input. From the location-based cooling rate and melt pool size, we conclude that except for the initial portion (x =20 to 28 mm), the control objective is well-achieved on the area of interest.

Another case of open-loop response is shown in Fig. 9, where the true $\alpha = 0.7$ is incorrectly known as $\hat{\alpha} = 0.6$. The input is optimized according to the wrong $\hat{\alpha}$ as $v = v^* = 180.30$ mm/min, $P = \bar{A}D\rho C_p p^* / \kappa = 757.93$ W. The simulation is terminated at $t = 21$ s. A steady-state different from U^* has been reached (Fig. 9(c)), resulting in deviation of both Cr and W from the desired values (Figs. 9(d) and 9(e)).

5.4 Closed-Loop Response With Known α. In this part, we show that the same control objective can be achieved by the proposed closed-loop control scheme integrating passivity-based output feedback and adaptation of v^*, p^*. A constant proportional gain is used for the passivity feedback. We assume that the heat transfer coefficient $\alpha = 0.7$ is known. Figure 10 shows the simulated results of using the PI control with $U^*(y)$ computed with the correct α. PI control gains, $(\mathcal{K}_v, \mathcal{K}_p, K_{I_v}, K_{I_p})$, are tuned to minimize both response time and overshoot of time-based cooling rate and melt pool size. The selected gains are presented in Table 3. Antiwindup strategies are applied for the integral control. The maximum laser power and scanning velocity are chosen as $P_{\max} = 2000$ W, $v_{\max} = 300$ mm min^{-1}. From Fig. 10(c), it is seen that $U(y, t) \rightarrow U^*(y)$. Figure 10(d) shows that a steady-state is reached in 2.3 s for $Cr(t)$ and 2.5 s for $W(t)$, significantly faster than in the open-loop response. As a result, the control objective is achieved in all area of interest except for the initial portion $x = 20$ to 25 mm, shorter than that in the open-loop case.

We also present another case of closed-loop response in Fig. 11 with α incorrectly known. With proportional-integral-like feedback applied, $U(y, t)$ converges to a steady-state (Fig. 11(c)) very close to $U^*(y)$. As a result, the steady-state melt pool size converges very close to the desired value (Figs. 11(e) and 11(f)). However, the cooling rate settled at 20% higher compared to the desired value, mainly due to the higher scanning speed than v^* reached at steady-state (Fig. 11(d)).

5.5 Closed-Loop Response With α Estimation. In practice, the heat transfer coefficient α may not be readily known and also may vary between different scans. Therefore, we further simulate a case with estimation of α integrated in the control loop. The true value is still chosen as $\alpha = 0.7$. Initially, $\hat{\alpha} = 0.6$, the same as the known but incorrect value shown in the previous cases. The same

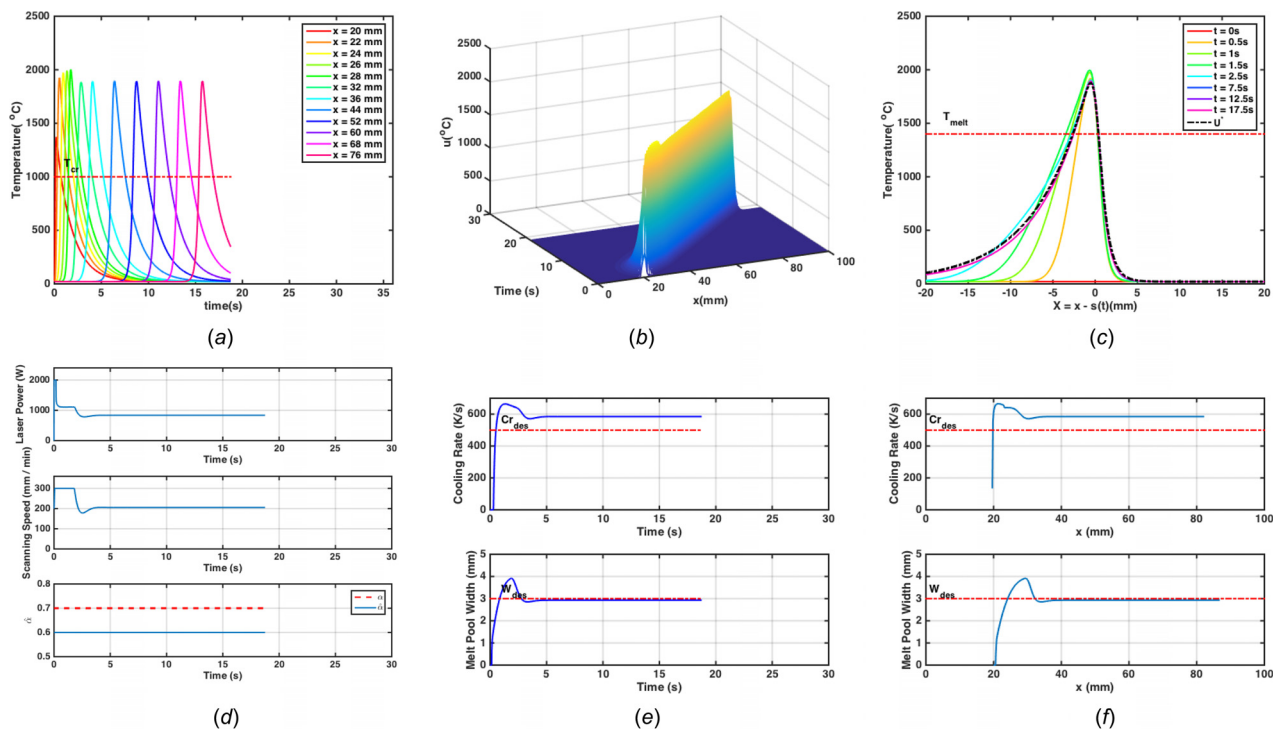(a)   (b)   (c)

(d)   (e)   (f)

Fig. 11 Closed-loop response where $U^*(y)$ is computed from $\hat{\alpha} = 0.6$ but the true $\alpha = 0.7$. (b) plots the full temperature field evolution. (a) and (c) plot, respectively, the temperature evolution at specific spatial location x's and the temperature distribution snapshots at specific time instance t's. (d) shows the input response. (e) plots the evolution of cooling rate and melt pool size. (f) shows the a posteriori spatial distribution of cooling rate and melt pool size. The area of interest for temperature control is from $x = 20$ mm to $x = 80$ mm.
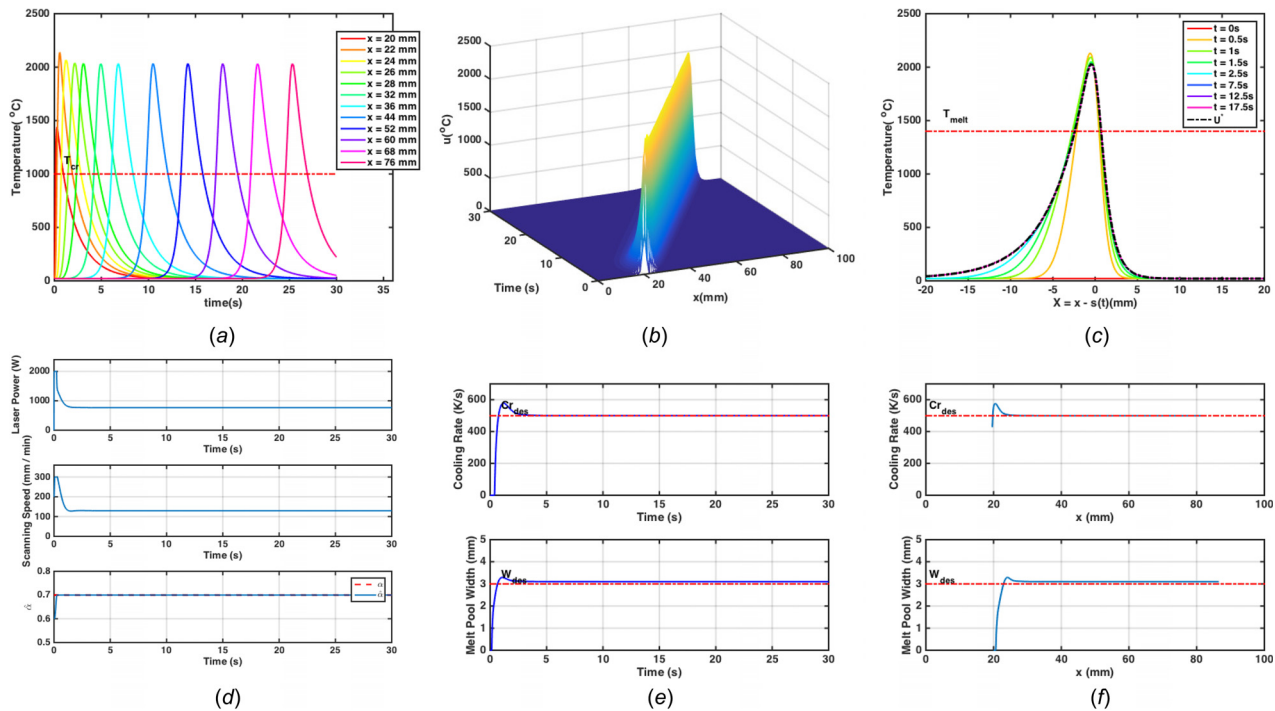
Fig. 12 Closed-loop response with α estimation incorporated. The unknown $\alpha = 0.7$, the initial guess of which starts from $\hat{\alpha} = 0.6$. (b) plots the full temperature field evolution. (a) and (c) plot, respectively, the temperature evolution at specific spatial location x's and the temperature distribution snapshots at specific time instance t's. (d) shows the input response, and the evolution of $\hat{\alpha}$. (e) plots the evolution of cooling rate and melt pool size. (f) shows the a posteriori spatial distribution of cooling rate and melt pool size. The area of interest for temperature control is from $x = 20$ mm to $x = 80$ mm.

PI gain selection as shown in Table 3 is applied. The estimator gains γ and K_e are tuned to minimize the response time of $\hat{\alpha}$, and are also included in Table 3. Simulation of the estimator PDE (28) is conducted based on finite difference method with $L = 50$ mm, a linear spacing of $\Delta y = 0.1$ mm, and the time increment of $\Delta t = 0.005$ s. Simulated results are plotted in Fig. 12. Convergence of $\hat{\alpha}$ is achieved within 0.5 s. Similar response time for $Cr(t)$ (2.5 s) and $W(t)$ (2 s) is demonstrated. As a result, the control objective is well achieved in all area of interest except for the initial portion $x = 20$ to 25 mm.

6 Conclusion

This paper presents a PDE-based approach to the thermal control problem in laser-based manufacturing. The control problem involves using the laser velocity and power to regulate the temperature in the moving laser frame to achieve the desired performance in terms of the cooling rate and melt pool size. We first show that the target temperature distribution corresponding to the desired performance is globally exponentially stable under a suitably chosen constant feedforward in laser velocity and power. A passive temperature error feedback, such as a proportional feedback gain, counteracts noise and model uncertainty while preserving stability. The feedforward itself may be adaptively updated resulting in an integral control term. Though the proportional-integral feedback is robust, the desired temperature distribution requires accurate model information. We construct an estimator for a key model parameter, the heat transfer coefficient to the ambient, to reduce the model dependence of the controller. Simulation results are presented for both known and unknown heat transfer coefficient to demonstrate the convergence of the cooling rate and melt pool size to the desired values.

Our current formulation is based on the 1D PDE model, which is a highly simplified description of the actual LAM process. In addition to the three-dimensional nature of thermal physics, there are other physical phenomena not addressed in the paper, such as the melting and solidification processes (which may be modeled using the Stefan condition [21,22]) and inaccurate material properties. The passivity based control methodology presented in this paper lays the foundation for our future work in controlling the LAM process in the more realistic 3D PDE model and ultimately experimental implementation.

Appendix A: Analytical Solution of the Steady-State Temperature Distribution in the Laser Frame

The steady-state solution of Eq. (9) satisfies

$$kU_{yy}^*(y) + v^* U_y^*(y) - \alpha U^*(y) + p^* \Pi(y) = 0 \qquad \text{(A1)}$$

which is a nonhomogeneous second-order ODE. The homogeneous part has two real eigenvalues

$$r_1 = \frac{-v^* + \sqrt{v^{*2} + 4k\alpha}}{2k}, \quad r_2 = \frac{-v^* - \sqrt{v^{*2} + 4k\alpha}}{2k}$$

The solution is the sum of the homogeneous and particular solutions

$$U^*(y) = e^{r_1 y}\left(c_1 + \int_{-L}^{y} w_1{}'(z)\,dz\right)$$
$$+ e^{r_2 y}\left(c_2 + \int_{-L}^{y} w_2{}'(z)\,dz\right) \tag{A2}$$

where

$$w_1'(y) = -\frac{p^*}{k(r_1 - r_2)}\Pi(y)e^{-r_1 y} \tag{A3}$$

$$w_2'(y) = \frac{p^*}{k(r_1 - r_2)}\Pi(y)e^{-r_2 y} \tag{A4}$$

Substituting in Eq. (A2) the boundary condition $U^*(-L) = U^*(L) = 0$ where L is large, and noting that $r_1 > 0$ and $r_2 < 0$, we get

$$c_1 \approx -\int_{-L}^{L} w_1'(y)\,dy \approx \int_{-\infty}^{\infty} w_1'(y)\,dy \tag{A5a}$$

$$c_2 \approx -\int_{-L}^{-L} w_2'(y)\,dy = 0 \tag{A5b}$$

If Π is the delta function

$$U^*(y) = \frac{p^*}{k(r_1 - r_2)}\left(1(-y)e^{r_1 y} + 1(y)e^{r_2 y}\right) \tag{A6}$$

where $1(\cdot)$ denotes the Heaviside function.

The solution for rectangular power distribution Π is

$$U^*(y) = \begin{cases} \dfrac{p^*\left(e^{\frac{r_1 D}{2}} - e^{-\frac{r_1 D}{2}}\right)}{kDr_1(r_1 - r_2)}e^{r_1 y}, & y < -\dfrac{D}{2} \\[3ex] \dfrac{p^*}{kD(r_1 - r_2)}\left(\dfrac{1 - e^{r_1\left(y - \frac{D}{2}\right)}}{r_1} + \dfrac{e^{r_2\left(y + \frac{D}{2}\right)} - 1}{r_2}\right), & -\dfrac{D}{2} \le y \le \dfrac{D}{2} \\[3ex] \dfrac{p^*\left(e^{\frac{r_2 D}{2}} - e^{-\frac{r_2 D}{2}}\right)}{kDr_2(r_1 - r_2)}e^{r_2 y}, & y > \dfrac{D}{2} \end{cases} \tag{A7}$$

Note that when $D \to 0$, Eq. (A7) approaches Eq. (A6). The solution for the Gaussian power distribution Π is

$$U^*(y) = \frac{p^*}{2k(r_1 - r_2)}\left\{\left\{ae^{\frac{r_2^2\sigma^2}{2} + r_2 y}\mathrm{erf}\left(\frac{y + \sigma^2 r_2}{\sqrt{2}\sigma}\right)\right.\right.$$
$$\left.\left. - e^{\frac{r_1^2\sigma^2}{2} + r_1 y}\left[\mathrm{erf}\left(\frac{y + \sigma^2 r_1}{\sqrt{2}\sigma}\right) - 1\right]\right\}\right\} \tag{A8}$$

where $\mathrm{erf}(\cdot)$ is the error function.

Appendix B: Analytical Expression of (Cr^*, W^*) as Functions of (v^*, p^*)

Given $U^*(y)$ from Appendix A, we can relate the steady-state performance measures (Cr^*, W^*) to the inputs (v^*, p^*). We will also explicitly highlight the dependence on the heat transfer

coefficient α, as it is typically the least determined component in the model. We will consider the case that $\Pi(y) = \delta(y)$ only, to obtain the analytical relationship. From Eq. (A6), we have

$$U^*(y_{\mathrm{cr}}) = \frac{p^*}{k(r_1 - r_2)}e^{r_1 y_{\mathrm{cr}}} = T_{\mathrm{cr}}$$

From Eq. (20), the steady-state cooling rate is given by

$$\mathrm{Cr}^* = U_y^*(y)\big|_{y = y_{\mathrm{cr}}}v^* = \frac{p^* r_1}{k(r_1 - r_2)}e^{r_1 y_{\mathrm{cr}}}v^* = r_1 v^* T_{\mathrm{cr}}$$
$$= \frac{T_{\mathrm{cr}}}{2k}v^*\left(-v^* + \sqrt{v^{*2} + 4k\alpha}\right) \tag{B1}$$

Solving v^*, we obtain

$$v^* = \sqrt{\frac{k}{T_{\mathrm{cr}}}}\frac{\mathrm{Cr}^*}{\sqrt{\alpha T_{\mathrm{cr}} - \mathrm{Cr}^*}} := f(\alpha, \mathrm{Cr}^*) \tag{B2}$$

which implies that Cr^* must be less than αT_{cr} (sufficiently slow cooling rate) in order for a feasible velocity to exist. For the melt pool size, first solve for the boundary locations of the melt pool

$$U^*(y_\ell) = U^*(y_r) = T_{\mathrm{melt}}, y_r > y_\ell$$

If there is no solution, then $W^* = 0$. Substituting in Eq. (A6), we have

$$\frac{p^*}{k(r_1 - r_2)}e^{r_1 y_\ell} = \frac{p^*}{k(r_1 - r_2)}e^{r_2 y_r} = T_{\mathrm{melt}}$$

This implies that

$$r_1 y_\ell = r_2 y_r$$

Then

$$W^* = y_r - y_\ell = \frac{r_1 - r_2}{r_1 r_2}\ln\left(\frac{T_{\mathrm{melt}}k(r_1 - r_2)}{p^s}\right) \tag{B3}$$

Solving for p^*, we obtain

$$p^* = T_{\mathrm{melt}}\sqrt{v^{*2} + 4k\alpha}\,\exp\left(\frac{\alpha W^*}{\sqrt{v^{*2} + 4k\alpha}}\right)$$
$$:= g(\alpha, v^*, W^*) \tag{B4}$$

Appendix C: Eigen-Solution of the Laplace Operator

Consider the eigenvalue problem corresponding to the Laplace operator

$$\phi_{xx} = -\lambda\phi, \quad \phi(0) = \phi(\ell) = 0 \tag{C1}$$

Since the Laplace operator is self-adjoint and negative semidefinite, its spectrum consists of nonpositive eigenvalues with eigenfunctions forming an orthonormal basis in $L^2(0, \ell)$ [34]. The eigen-solution is given by solving Eq. (C1) and normalizing ϕ

$$\lambda_n = \left(\frac{n\pi}{2\ell}\right)^2, \quad n \ge 0$$

$$\phi_n(x) = \begin{cases} \dfrac{1}{\sqrt{2\ell}}\sin\left(\dfrac{n\pi(x + \ell)}{2\ell}\right) & n > 0 \\[3ex] \dfrac{1}{\sqrt{2\ell}} & n = 0 \end{cases} \tag{C2}$$

References

[1] Gu, D., Hagedorn, Y.-C., Meiners, W., Meng, G., Batista, R. J. S., Wissenbach, K., and Poprawe, R., 2012, "Densification Behavior, Microstructure Evolution, and Wear Performance of Selective Laser Melting Processed Commercially Pure Titanium," Acta Mater., 60(9), pp. 3849–3860.

[2] Griffith, M. L., Ensz, M. T., Puskar, J. D., Robino, C. V., Brooks, J. A., Philliber, J. A., Smugeresky, J. E., and Hofmeister, W. H., 2000, "Understanding the Microstructure and Properties of Components Fabricated by Laser Engineered Net Shaping (Lens)," MRS Proc., 625, p. 9.

[3] Farshidianfar, M. H., Khajepour, A., and Gerlich, A., 2016, "Real-Time Control of Microstructure in Laser Additive Manufacturing," Int. J. Adv. Manuf. Technol., 82(5–8), pp. 1173–1186.

[4] Nie, P., Ojo, O., and Li, Z., 2014, "Numerical Modeling of Microstructure Evolution During Laser Additive Manufacturing of a Nickel-Based Superalloy," Acta Mater., 77, pp. 85–95.

[5] Sateesh, N., Kumar, G. M., Prasad, K., C.K, S., and Vinod, A., 2014, "Microstructure and Mechanical Characterization of Laser Sintered Inconel-625 Superalloy," Procedia Mater. Sci., 5, pp. 772–779.

[6] Kelly, S. M., 2004, "Thermal and Microstructure Modeling of Metal Deposition Processes With Application to Ti-6Al-4V," Ph.D. thesis, Virginia Tech, Blacksburg, VA.

[7] Ikeda, T., Ravi, V. A., and Jeffrey Snyder, G., 2010, "Microstructure Size Control Through Cooling Rate in Thermoelectric PbTe-Sb$_2$Te$_3$ Composites," Metall. Mater. Trans. A, 41(3), pp. 641–650.

[8] Simchi, A., and Pohl, H., 2003, "Effects of Laser Sintering Processing Parameters on the Microstructure and Densification of Iron Powder," Mater. Sci. Eng.: A, 359(1–2), pp. 119–128.

[9] Humphreys, F. J., and Hatherly, M., 2012, Recrystallization and Related Annealing Phenomena, Elsevier, Oxford, UK.

[10] Farshidianfar, M. H., Khajepour, A., and Gerlich, A. P., 2016, "Effect of Real-Time Cooling Rate on Microstructure in Laser Additive Manufacturing," J. Mater. Process. Technol., 231, pp. 468–478.

[11] Rosenthal, D., 1941, "Mathematical Theory of Heat Distribution During Welding and Cutting," Weld. J., 20(5), pp. 220s–234s.

[12] Poorhaydari, K., Patchett, B., and Ivey, D., 2005, "Estimation of Cooling Rate in the Welding of Plates With Intermediate Thickness," Weld. J., 84(10), pp. 149s–155s.

[13] Mayboudi, L. S., 2008, "Heat Transfer Modelling and Thermal Imaging Experiments in Laser Transmission Welding of Thermoplastics," Ph.D. thesis, Queen's University, Kingston, ON, Canada.

[14] Doumanidis, C., and Hardt, D., 1990, "Simultaneous in-Process Control of Heat Affected Zone and Cooling Rate During Arc Welding," Weld. J., 69(5), pp. 186s–196s.

[15] Kumar, K. S., 2014, "Analytical Modeling of Temperature Distribution, Peak Temperature, Cooling Rate and Thermal Cycles in a Solid Work Piece Welded by Laser Welding Process," Procedia Mater. Sci., 6, pp. 821–834.

[16] Kundakcioglu, E., Lazoglu, I., and Rawal, S., 2016, "Transient Thermal Modeling of Laser-Based Additive Manufacturing for 3D Freeform Structures," Int. J. Adv. Manuf. Technol., 85(1–4), pp. 493–501.

[17] Okamura, I., 1994, "Control Using Neural Networks and Adaptive Control for Cooling Rate in GMA Welding," Ph.D. thesis, Massachusetts Institute of Technology, Cambridge, MA.

[18] Doumanidis, C., and Hardt, D. E., 1991, "Multivariable Adaptive Control of Thermal Properties During Welding," ASME J. Dyn. Syst. Meas. Control, 113(1), pp. 82–92.

[19] Sammons, P., Bristow, D., and Landers, R., 2018, "Two-Dimensional Modeling and System Identification of the Laser Metal Deposition Process," ASME. J. Dyn. Syst. Meas. Control, 141(2), p. 021012.

[20] Sammons, P. M., Gegel, M. L., Bristow, D. A., and Landers, R. G., 2019, "Repetitive Process Control of Additive Manufacturing With Application to Laser Metal Deposition," IEEE Trans. Control Syst. Technol., 27(2), pp. 566–575.

[21] Koga, S., Diagne, M., and Krstic, M., 2016, "Output Feedback Control of the One-Phase Stefan Problem," IEEE 55th Conference on Decision and Control (CDC), Las Vegas, NV, Dec. 12–14, pp. 526–531.

[22] Koga, S., Diagne, M., Tang, S., and Krstic, M., 2016, "Backstepping Control of the One-Phase Stefan Problem," American Control Conference (ACC), Boston, MA, July 6–8, pp. 2548–2553.

[23] Unocic, R. R., and DuPont, J. N., 2004, "Process Efficiency Measurements in the Laser Engineered Net Shaping Process," Metall. Mater. Trans. B, 35(1), pp. 143–152.

[24] Li, S., Xiao, H., Liu, K., Xiao, W., Li, Y., Han, X., Mazumder, J., and Song, L., 2017, "Melt-Pool Motion, Temperature Variation and Dendritic Morphology of Inconel 718 During Pulsed-and Continuous-Wave Laser Additive Manufacturing: A Comparative Study," Mater. Des., 119, pp. 351–360.

[25] Jin, B., Liu, W., and Ohshima, K., 1995, "Control of Weld Pool Width and Cooling Rate in Circumferential GTA Welding of a Pipe by Using Neural Network Model," Proceedings IEEE Conference on Industrial Automation and Control Emerging Technology Applications, Taipei, Taiwan, May 22–27, pp. 41–46.

[26] Aggarangsi, P., Beuth, J. L., and Griffith, M. L., 2003, "Melt Pool Size and Stress Control for Laser-Based Deposition Near a Free Edge," Solid Freeform Fabrication Symposium, Austin, TX, Aug. 4–6, pp. 196–207.

[27] Khalil, H. K., 2002, Nonlinear Systems, Prentice Hall, Upper Saddle River, NJ.

[28] Spears, T., and Gold, A., 2016, "In-Process Sensing in Selective Laser Melting (SLM) Additive Manufacturing," Integr. Mater. Manuf. Innovation, 5(1), pp. 16–25.

[29] Chivel, Y., and Smurov, I., 2010, "On-Line Temperature Monitoring in Selective Laser Sintering/Melting," Phys. Procedia, 5, pp. 515–521.

[30] Berumen, S., Bechmann, F., Lindner, S., Kruth, J., and Craeghs, T., 2010, "Quality Control of Laser and Powder Bed-Based Additive Manufacturing (AM) Technologies," Phys. Procedia, 5, pp. 617–622.

[31] Craeghs, T., Clijsters, S., Yasa, E., and Kruth, J., 2011, "Online Quality Control of Selective Laser Melting," 22nd Annual International Solid Freedom Fabrication Symposium, Vol. 5, Austin, TX, Aug. 8–10, pp. 212–226.

[32] Grasso, M., Laguzza, V., Semeraro, Q., and Colosimo, B., 2016, "In-Process Monitoring of Selective Laser Melting: Spatial Detection of Defects Via Image Data Analysis," ASME. J. Manuf. Sci. Eng., 139(5), p. 051001.

[33] Clijsters, S., Craeghs, T., Buls, S., Kempen, K., and Kruth, J., 2014, "In Situ Quality Control of the Selective Laser Melting Process Using a High-Speed, Real-Time Melt Pool Monitoring System," Int. J. Adv. Manuf. Technol., 75(5–8), pp. 1089–1101.

[34] Naylor, A. W., and Sell, G. R., 2000, Linear Operator Theory in Engineering and Science, Springer Science & Business Media, New York.